Research Square

Preprints are preliminary reports that have not undergone peer review.
They should not be considered conclusive, used to inform clinical practice,
or referenced by the media as validated information.

The SUMO isopeptidase activity of SENP7 can sustain the expression of developmental genes but not a repressive state on chromosome X

Mario García-Domínguez

mario.garcia@cabimer.es

CABIMER - CSIC https://orcid.org/0000-0003-2211-8731

Vahid Jafari

CABIMER (CSIC) https://orcid.org/0000-0002-4970-0011

Belén Torres

CABIMER

Lorena García-Bernal

CABIMER - CSIC

Nieves Lara-Ureña

CABIMER - CSIC

María Arroyo

Technical University of Darmstadt

José Carlos Reyes

CABIMER / CSIC https://orcid.org/0000-0002-8042-5142

M Cristina Cardoso

echnische Universität Darmstadt https://orcid.org/0000-0001-8427-8859

Article

Keywords: sumoylation, SENP7, catalytic domain, development, neurogenesis, chromosome X

Posted Date: August 6th, 2026

DOI: https://doi.org/10.21203/rs.3.rs-10456151/v1

License: This work is licensed under a Creative Commons Attribution 4.0 International License.
Read Full License

Additional Declarations: There is no duality of interest

Abstract

Sumoylation consists of the covalent attachment of the SUMO polypeptide to proteins and is essential in mammals, in which it controls virtually all cellular processes. The specific SUMO proteases of the SENP family are key regulators of the process. Among them, SENP7 and SENP6 are unique in having a split catalytic domain involved in depolymerizing SUMO2/3 polySUMO chains. Besides, they have long N-terminal regions poorly studied to date. In this study, we have analyzed cells lacking SENP7 to investigate alterations in the transcription profile and chromatin structure. Interestingly, we observe a significant downregulation of development-related genes, especially those associated with the nervous system, and a modest upregulation of chromosome X genes. This correlates with disturbed DNA compaction and histone modification profile. In the *SENP7* knockout background, we have stably expressed the catalytic domain alone, which notably rescues the expression of developmental genes and restores DNA compaction and the histone modification profile. However, it does not suffice to reestablish the expression of chromosome X genes, uncovering a relevant role for SENP7 in chromosome X architecture, which absolutely requires its N-terminal region. Remarkably, the levels of two key players of chromosome X inactivation, the long non-coding RNA *XIST* and the histone variant macroH2A, which are downregulated in knockout cells, do not recover in the stable cell line expressing the catalytic domain. Thus, we propose a dual role for SENP7. For an important set of developmental genes, its isopeptidase activity facilitates chromatin opening, while for another set of genes, its N-terminal region is required for the stabilization of a repressive state, which is particularly manifest in chromosome X.

INTRODUCTION

Accurate orchestration of cellular processes is crucial during development and in response to internal and external cues. Thus, signaling mechanisms are essential pathways for healthy cell physiology. In this context, sumoylation, the post-translational modification of proteins by covalent attachment of SUMO polypeptides, is a signaling mechanism gaining increasing relevance [1]. Sumoylation occurs at K residues in proteins, often embedded in the consensus sequence YKxE/D, where Y is a long-chain hydrophobic residue and x is any residue. Three main SUMO polypeptides have been described in vertebrates: SUMO1-3. SUMO2 and SUMO3 are almost identical and cannot be distinguished by antibodies, so they are commonly referred to as SUMO2/3. In contrast to SUMO1, SUMO2/3 is more likely to form poly-SUMO chains, due to the presence of the sumoylation consensus in its sequence. SUMO attachment to targets requires the action of activating (the heterodimer SAE1/UBA2) and conjugating (UBC9) enzymes, and frequently the participation of SUMO ligases, promoting or enhancing SUMO transfer to targets [2]. However, especially relevant are SUMO proteases, not only because they are necessary for maturation of the SUMO precursors, but because they are essential for detaching SUMO molecules from targets, enabling SUMO recycling.

The most studied SUMO-specific proteases are those of the SENP family: SENP1-3, 5–7 [3], which are considered main regulators of the sumoylation process. Among them, SENP6 and SENP7 have the

peculiarity of presenting a split catalytic domain at the C-terminus, and are specialized in depolymerizing poly-SUMO2/3 chains [4, 5]. Besides, they also present a long N-terminal region poorly characterized. SENP6 has been related to the DNA damage response and to chromatin organization, in particular to spindle assembly and centromere structure [6–10]. In turn, SENP7 has been associated with development, the immune response, chromatin organization and cell viability [11–24]. However, the exact mechanisms and targets through which they perform many of their functions remain largely unknown.

To shed light on this matter, we have focused on SENP7 and have analyzed in detail knockout (KO) cells generated in the HAP1 cell line. We found that loss of SENP7 results in marked gene repression, although a set of genes modestly upregulated also appeared. We previously described the requirement for SENP7 for proper neuronal differentiation in P19 cells and vertebrate embryos [17]. However, no SENP7-dependent genes were identified. We have now identified specific genes, most of them related to nervous system development, but also to additional developmental processes. The observed gene misregulation correlates with an altered histone modification pattern in KO cells. Interestingly, we have also observed a modest but consistent and extensive upregulation of genes on chromosome X (chrX). More importantly, stable expression of the SENP7 catalytic domain in the KO background vastly rescues misregulation of development-related genes, but it is not able to restore upregulation of chrX-associated genes, suggesting a functional decoupling between catalytic and N-terminal regions of SENP7.

RESULTS

SENP7 depletion leads to downregulation of developmental genes

To delve into the function of SENP7, we decided to analyze transcriptional alterations linked to its absence. To this purpose, we studied *SENP7* KO cells raised in the human HAP1 cell line by a CRISPR/Cas9 approach. These cells were designated as KO1, and they resulted from targeting of exon 4, leading to a 10-bp deletion, provoking a frameshift resulting in the appearance of an early STOP codon, whether exon 5 is retained or skipped (Supplementary Fig. S1). We proceeded to analyze the transcriptome of parental HAP1 cells and KO1 mutant cells by RNA sequencing (RNA-seq), and Principal Component Analysis (PCA) indicated notable differences between HAP1 and KO1 cells, and also high similarity between replicas (Supplementary Fig. S2A). Volcano plot showed a remarkable downregulation of genes (Fig. 1A and Supplementary Dataset S1). The upregulated genes were somewhat less numerous and showed a fairly modest fold change (FC). To reinforce these observations, we analyzed a second KO line, also raised by targeting exon 4 and presenting a 10-bp deletion, but located downstream of that of KO1 cells. This mutation resulted again in the appearance of an early STOP codon, regardless of the processing of exon 5 (Supplementary Fig. S1); these cells were designated as KO2. PCA of RNA-seq data showed a clear proximity between KO2 and KO1 cells, especially in the first dimension (Supplementary Fig. S2A), and volcano plot of KO2 misregulated genes was quite similar to that of KO1

misregulated genes (Supplementary Fig. S2B and Supplementary Dataset S1). Overlapping of misregulated genes between KO1 and KO2 cells, either upregulated or downregulated, was noticeably high, with a fold enrichment greater than 12 (Fig. 1B). Gene Ontology (GO) analysis of misregulated genes, both upregulated and downregulated, notably grouped a significant number of genes in the categories of *neurogenesis* and *nervous system development* but also in *circulatory system development* (Fig. 1C). Regarding upregulated genes, they were specially related to neuronal projections, axons and dendrites, while downregulated genes also grouped into additional developmental categories, like *gliogenesis*, *skeletal system development*, and *lung development* (Fig. 1C). In addition, among misregulated genes, we also observed some genes related to the *inflammatory response* (Fig. 1A). We selected some genes for validation through quantitative RT-PCR (RT-qPCR), which confirmed the RNA-seq results (Fig. 2). Although many of these genes shared several GO categories (Supplementary Fig. S2C), in Fig. 2, we tried to group them into categories related to their major described functions.

Thus, the absence of SENP7 mainly leads to the misregulation of development-related genes.

Chromosome X-associated genes are consistently upregulated in the absence of SENP7

Despite the modest FC of upregulated genes, we surprisingly noticed a high number of these belonging to the chrX (Fig. 1A). Plot of chromosome distribution of upregulated genes in KO1 cells clearly indicated a severe discrepancy between expected and observed values for chrX (Fig. 3A). Moreover, upregulated genes were uniformly distributed along the chrX (Fig. 3B). Of the hundreds of genes located in chrX, in our RNA-seq analysis we detected expression of 695, being 102 of these among the genes upregulated in KO1 cells, which represents a significant 3.4-fold enrichment as determined by the hypergeometric test (Fig. 3C). Similar observations were made in the case of KO2 cells (Supplementary Figs. S2B and S3A-C). Volcano plot of the 695 chrX detected genes indicated that in KO1 cells, in comparison with 102 upregulated genes, very few (36 genes) were downregulated, while the rest of the genes remained unaltered (Supplementary Fig. S3D). Moreover, considering the commonly misregulated genes between KO1 and KO2 cells, the overlapping of upregulated genes with the 695 chrX expressed genes reached a fold enrichment of more that 4, while the overlapping of downregulated genes was not significant and did not represent any enrichment (Supplementary Fig. S3E). We already validated by RT-qPCR the expression levels of *TMEM47*, located in chrX, in the different cell lines (Fig. 2), but we selected more chrX genes for validation by RT-qPCR, which showed increased expression in both KO cell lines compared with parental HAP1 cells (Fig. 3D). Since HAP1 cells are haploid cells that may tend to partially diploidize over time [25], which could explain the higher expression of certain genes when comparing different sets of cells, we performed experiments to compare the relative levels of genomic content in the different cell lines. Thus, we conducted qPCR analyses on genomic DNA to evaluate two of the chrX *loci* already analyzed by RT-qPCR (*ARX*, *TMEM47*) and a third non-related *locus* located on chr2 (*KCNK3*). Results showed similar genomic content in parental and KO cell lines, discarding possible genome duplications (Fig. 3E).

These results uncover an unexpected role of SENP7 in maintaining a repressive state on chrX.

Expression of the catalytic domain of SENP7 significantly rescues the expression of developmental genes

As explained, in addition to possessing a split catalytic domain at the C-terminus, SENP7 exhibits an unusually long N-terminal region that has been little explored functionally to date. Therefore, we questioned the necessity of this region for the function of SENP7. To analyze whether the N-terminal region is dispensable, we proceeded to complement KO cells with just the catalytic domain. To this purpose, we prepared an expression construct involving just the SENP7 catalytic domain, with an AM tag at its C-terminus. As features for nuclear localization of SENP7 localize to the N-terminal region, as determined by the NLSExplorer tool, we also included a canonical nuclear localization signal (NLS) from the SV40 large T-antigen, at the N-terminus of our catalytic domain construct (Fig. 4A). We checked for nuclear localization of the expressed construct in HAP1 cells (Supplementary Fig. S4A). We introduced this construct in KO1 cells and selected for its stable integration into the genome in the presence of puromycin. We obtained several resistant clones, and we selected clone #5, which stably expressed the catalytic domain, for further analysis (Fig. 4B); these cells were designated KOCt1. The gene expression profile of these cells was analyzed by RNA-seq, and PCA indicated that, although they were not identical to parental HAP1 cells, they were closer to HAP1 cells than to KO cells in the first dimension, suggesting partial rescue of the phenotype (Supplementary Fig. S2A). In contrast to KO1 cells, the volcano plot did not show a predominant gene downregulation, and gene upregulation was more pronounced than in KO1 cells, with the number of misregulated genes quite higher in the new cells (Fig. 4C and Supplementary Dataset S1). Both upregulated and downregulated genes were again associated with the GO category of *circulatory system development* (Fig. 4D). However, the top GO categories for upregulated genes were related to *nervous system development*, though not to axons and dendrites. In contrast, the grouping of downregulated genes in these categories was less evident (Fig. 4D). When we compared genes upregulated or downregulated in KO1 cells with genes showing the opposite behavior in KOCt1 cells relative to KO1 cells, we found a stronger enrichment for genes that were downregulated in KO1 cells and subsequently upregulated in KOCt1 cells than for genes that were upregulated in KO1 cells and subsequently downregulated in KOCt1 cells (Fig. 5A). This indicates that expression of the catalytic domain preferentially rescues genes whose expression is reduced in KO1 cells. In particular, of 893 genes downregulated in KO1 cells, 341 appeared upregulated in KOCt1 cells when compared with KO1 cells (Fig. 5A). GO analysis of these 341 genes showed a grouping essentially into developmental categories (Supplementary Fig. S4B). RNA-seq-based heatmap of the expression of development-related genes showed that while genes downregulated in KO1 cells were in general significantly upregulated in KOCt1 cells, most of the genes upregulated in KO1 cells remained upregulated in KOCt1 cells (Fig. 5B). Specifically related to the category of *nervous system development*, scatter plots indicated that when analyzing how the 139 upregulated and 144 downregulated genes in KO1 cells are in KOCt1 cells, significant differences for mean FC values were only observed for downregulated genes, less affected in KOCt1 cells (Fig. 5C). Thus, expression of the catalytic domain in KO1 cells notably alleviates the

downregulation of developmental genes, especially those related to neurodevelopment. This is also observed in volcano plots of misregulated genes in the *nervous system development* category from both cell lines. Notably, many downregulated genes in KO1 cells appear close to the midline in KOCt1 cells (Supplementary Fig. S4C). The expression of selected genes was validated by RT-qPCR, showing a prominent rescue of the expression of most developmental genes in KOCt1 cells (Fig. 5D). Some genes, like SYK and TAL1, displayed partial rescue, while expression of genes related to the *inflammatory response* was not restored (Fig. 5D). We analyzed an additional stable clone expressing the SENP7 catalytic domain, clone #9, designated as KOCt2 (Supplementary Fig. S4D) to validate expression of selected genes by RT-qPCR (Supplementary Fig. S4E).

Therefore, our results indicate that the catalytic domain of SENP7 is sufficient to maintain the expression of developmental genes, and that the rest of the protein is largely dispensable for this.

The catalytic domain of SENP7 stimulates neuronal differentiation

Next, we wondered about the capacity of the catalytic domain to alter neurogenesis when overexpressed. To this end, we used an overexpression construct of the catalytic domain based on the RSV promoter to study neurogenesis in P19 cells, a pluripotent model cell line that differentiates into neurons when transfected with expression constructs for neurogenic factors [26]. Transient transfection of expression constructs for the neurogenic factor Neurod2 and its cofactor E12 causes 10% of the cells in the plate to express the neuronal marker ßIII-tubulin in P19 cells (Fig. 6A). Interestingly, overexpression of the catalytic domain together with Neurod2 notably increased neurogenesis, while overexpression of full-length SENP7 stimulated neurogenesis to a lesser extent (Fig. 6A). We then asked about the neurogenic potential of the SENP7 catalytic domain in the absence of neurogenic factors. To analyze this, we turned to forced expression of our construct in the developing neural tube through in vivo electroporation of the chick embryo. Electroporation allows for the efficient transfection of one half of the neural tube after the injection of DNA into its lumen and the application of an electrical pulse. The non-electroporated half serves as a control for the experiment. In the developing neural tube, neuronal progenitors proliferate in the ventricular zone (VZ), near the lumen of the tube, and progressively exit the cell cycle and migrate to the margins of the tube, the mantle layer (ML), where they settle to complete their differentiation and express the neuronal marker ßIII-tubulin (Fig. 6B, left panel). This process can be accelerated by forced expression of the neurogenic factor Neurogenin-2 (Neurog2), which causes more than 90% of the electroporated cells, monitored by expression of GFP from a co-electroporated reporter vector, to be located in the ML and to express βIII-tubulin (Fig. 6C, left panel). However, in the absence of Neurog2, overexpression of the catalytic domain of SENP7 significantly stimulated naturally occurring neurogenesis, as more cells migrated to the ML in relation to the control condition (empty vector) (Fig. 6B). In the context of neurogenesis, we also wondered about the effects of the N-terminal region of SENP7. Since no special domains have been defined in this region, except for two small motifs interacting with the heterochromatin protein HP1 [20], we decided to express a construct including these two motifs, corresponding to amino acids 1 to 308 of SENP7. Expression of this fragment in P19 cells

under Neurod2-mediated neurogenesis induction conditions resulted in reduced neurogenesis compared with control conditions (Fig. 6A). Similar results were observed under Neurog2-induced neurogenesis conditions in the embryonic neural tube (Fig. 6C), suggesting a dominant-negative effect of the N-terminal construct.

In sum, we have shown that overexpression of the isolated catalytic domain of SENP7 can stimulate neurogenesis in P19 cells and embryos.

SENP7 depletion leads to altered chromatin compaction and histone modifications

Since SENP7 has been linked to chromatin dynamics [15, 19, 20], we decided to analyze chromatin state in KO cells. We first performed quantitative analyses of 3D nuclear landscape and DNA compaction by confocal microscopy on DAPI-stained cells. Using a segmentation algorithm, DAPI signals from DNA-stained cells were divided into seven defined intensity classes with similar variance, from less intensity and more relaxed chromatin organization in Class 1 to the highest level of chromatin condensation and compaction in Class 7 [27]. We observed that KO1 cells showed a higher fraction of compacted classes than the parental HAP1 cells (Fig. 7A). Interestingly, in KOCt1 cells, the compaction pattern was restored to values almost identical to those of parental cells (Fig. 7A). We then analyzed the general display of corresponding histone modifications by high-content fluorescence microscopy. Acetylation of Lys9 (H3K9ac) or Lys27 (H3K27ac) on histone H3 is indicative of open transcriptionally active regions. In particular, H3K27ac is strongly associated with active enhancers and promoters. On the other hand, trimethylation of these residues is linked to repression. H3K27me3 is particularly associated with facultative heterochromatin and is established by the Polycomb Repressive Complex 2 (PRC2), while H3K9me3 is also found in constitutive heterochromatin and is established by several histone methyltransferase complexes. Surprisingly, all these modifications were reduced in KO1 cells, both acetylation and trimethylation, and more importantly, they were restored in KOCt1 cells, to levels similar to those of the parental cells in the case of trimethylation, and even to values higher than those of parental cells in the case of acetylation (Fig. 7B).

Thus, loss of SENP7 leads to an altered chromatin state, but reintroduction of only the catalytic domain of SENP7 appears to restore chromatin architecture.

The catalytic domain of SENP7 is unable to restore the expression of Chromosome X-associated genes

Since we observed a peculiar behavior of chrX genes in KO1 cells, we decided to analyze in more detail how chrX genes are expressed in KOCt1 cells. Surprisingly, we observed that most of the 102 genes located in chrX, which were modestly upregulated in KO1 cells, also appeared modestly upregulated in KOCt1 cells (Fig. 8A). In fact, the mean upregulation value (FC) of these 102 genes in KOCt1 cells was

not different from that in KO1 cells (Fig. 8B). We checked by RT-qPCR a selection of genes to corroborate that these appeared as upregulated in KOCt1 as in KO1 cells (Fig. 8C), with no significant differences between them (Fig. 8C). We analyzed two of these genes also in KOCt2 cells with similar results (Supplementary Fig. S4E). The histone variant macro H2A (mH2A), involved in gene silencing because it contributes to the formation of dense repressed chromatin, is enriched in chromatin of the inactive chrX in mammals [28]. We sought to analyze the levels of this histone variant in our different cells, and interestingly found that they were reduced in KO1 cells compared to parental HAP1 cells, and remained reduced in KOCt1 cells (Fig. 8D). Another major determinant of chrX condensation is the long non-coding RNA (lncRNA) *XIST*, which is expressed to coat the chrX copy to be inactivated [29]. Expression analyses of this lncRNA in KOCt1 cells showed reduced levels of expression, compared to parental cells, and similar to those of KO1 cells (Fig. 8E), in agreement with former observations.

In sum, although expression of the SENP7 catalytic domain in KO1 cells roughly restores general chromatin structure and expression of developmental genes, the altered expression of chrX genes remains unaffected.

DISCUSSION

Since sumoylation is essential for survival across almost all eukaryotes, the study of its specific regulators acquires notable relevance. Sumoylation acts on thousands of proteins, being involved in the regulation of virtually all cellular processes. Such a vast scenario requires fine and accurate tuning. The main regulators of sumoylation are ligases and proteases. Ligases have been shown to exhibit an elevated degree of promiscuity, not only because some of them can target a variety of proteins for enhanced sumoylation, but also because they can display additional non-SUMO-related functions [30]. Conversely, SUMO proteases present a well-defined SUMO-specific activity and are essential for SUMO maturation and recycling, which is necessary to maintain cell homeostasis [31]. Two of the SUMO proteases described to date are unique in having specialized in depolymerizing poly-SUMO2/3 chains, coincident with the presence of a split catalytic domain [4, 5]. Besides, they have atypical, poorly characterized long N-terminal regions preceding the C-terminal catalytic domain. Here, we describe how the lack of one of these proteases, SENP7, leads to altered chromatin features and transcriptional profile. This indicates that despite the similarities between SENP7 and its counterpart SENP6, the latter does not compensate for the loss of the former. More importantly, we report that the singular catalytic activity of SENP7 alone, in the absence of the long N-terminal region, is largely sufficient to restore the altered phenotype.

Loss of SENP7 leads to a marked decrease in gene expression. Among downregulated genes, a high number grouped into the GO category of *nervous system development*. The patent neurodevelopmental phenotype of *SENP7* KO cells is shocking, since HAP1 cells have a myeloid leukemia origin, which may align with the grouping of misregulated genes in the category of *circulatory system development*, as also happens. Nonetheless, altered expression of neurogenesis-related genes agrees with our previous report, indicating that SENP7 is required for proper progression of neurogenesis [17]. Moreover, the

developmental phenotype of KO cells extended beyond the nervous system, as misregulated genes also grouped in the categories of *circulatory system development*, as mentioned, *gliogenesis*, *skeletal system development* and *lung development*. Noticeably, these categories, together with that of *nervous system development*, fit quite well with the phenotypic features described in the first report of the *SENP7* mutation in humans, in which we participated [21]. Although in this study it was not possible to exclude the synthesis of a truncated peptide encompassing part of the N-terminal region, the probands displayed early respiratory failure and altered immune function, hematopoiesis, and development of nervous and skeletal systems, presenting with arthrogryposis multiplex congenita, neutropenia, and recurrent infections, which cause death in the first months of life [21]. These phenotypes have been confirmed in subsequent publications of additional cases [32–35].

The only well-defined domain in SENP7 is the C-terminal catalytic domain. Besides, two small patches of 5 amino acids in its N-terminal region have been proposed to stabilize the HP1 protein at pericentric heterochromatin [20]. Since we desired to evaluate the requirement of the N-terminal region for SENP7 function, we reintroduced just the catalytic domain in the KO background to be stably expressed. Expression of the isolated catalytic domain of a SENP member has been previously used for efficient protein desumoylation [36]. Surprisingly, expression of the SENP7 catalytic domain largely rescued the expression of developmental genes, especially regarding neurodevelopment, indicating that the N-terminal region was not substantially required. According to this, ectopic expression of the catalytic domain in P19 cells and in embryos resulted in enhanced neurogenesis. Despite the enhancement, data do not support neurogenic activity of the catalytic domain, as the stimulation was far from that achieved by true neurogenic factors such as Neurog2. To a lesser extent, likely due to differences in expression levels, the use of full-length SENP7 also enhanced neurogenesis. Conversely, ectopic expression of an N-terminal fragment of SENP7 impaired neurogenesis. Since this fragment contains the HP1 protein-interacting motifs proposed to mediate chromatin association of SENP7 [20], one possibility is that it displays a dominant-negative effect by displacing endogenous full-length SENP7 from the chromatin, blocking access to its targets. Although we observed that some markers related to *circulatory system development* did not reach parental values in stable cells, they showed increased expression in relation to KO cells. By contrast, some *inflammatory response*-related genes remained downregulated, indicating that their regulation requires the N-terminal region or the full-length protein. In line with the manifest transcriptional rescue, expression of the catalytic domain was also able to extensively reestablish the chromatin state, restoring DNA compaction values to those of parental cells, and allowing histone H3 methylation and acetylation values to reach or even exceed parental values, respectively. We also observed upregulation of some neurodevelopment-related genes in KO cells, but it was modest, and importantly, the mean FC value for these genes was not different after expressing the catalytic domain in KO cells. We then conclude that a major function of SENP7 is to support the expression of developmental genes, and that this essentially requires its catalytic activity.

More prominent than the modest induction of developmental genes is the also modest induction of dozens of genes (three times more than expected) located on chrX. These genes appeared evenly distributed all along the chrX, suggesting a general alteration of the chromosome architecture. Notably,

gene induction correlated with the decrease of the major determinant of chrX inactivation, *XIST* [29], and global reduction of the histone variant mH2A1, which also participates in chrX inactivation [28]. Since HAP1 cells are essentially haploid, chrX inactivation is not expected to occur on its only copy. However, partial inactivation of the chrX has been documented in a haploid context [37], consistent with modest upregulation when inactivating mechanisms are compromised. Notably, upregulation of chrX genes cannot be reverted by expression of the catalytic domain. According to this, mH2A1 and *XIST* levels remained unchanged in our stable cell line compared with KO cells. This suggests that proper regulation of chrX genes requires features of the N-terminal region. This region contains the interaction motifs for HP1, which recognizes and binds H3K9me3, a histone modification increasing during chrX inactivation [38]. Thus, it is tempting to speculate that these motifs are involved in maintaining chrX structure. Indeed, we have explained that our N-terminal construct containing these motifs probably displays a dominant-negative effect and that the H3K9me3 histone mark decreases in the absence of SENP7. Since the catalytic domain globally restores H3K9me3 but not chrX gene expression, one possibility is that, selectively, this mark is not properly stabilized on chrX in the absence of N-terminal SENP7, or that additional features in the 731 N-terminal amino acids account for relevant aspects of chrX dynamics.

SENP7 has been implicated in both heterochromatin stabilization through HP1 locking [20] and chromatin relaxation for DNA repair [15], which raises the question of whether it associates with open or closed chromatin. Our transcriptomic analysis revealed marked downregulation and modest upregulation of genes in its absence, indicating that SENP7 is predominantly required for gene expression. Unexpectedly, gene downregulation correlated with a reduction in repressive histone modifications (H3K9me3, H3K27me3), normally associated with more open chromatin and, consequently, with higher gene expression. However, histone acetylation marks associated with active transcription, such as H3K9ac and H3K27ac, were also reduced. Thus, SENP7 loss does not appear to simply shift chromatin toward a more permissive state. Rather, it generates an atypical chromatin configuration in which the reduction of repressive features is not accompanied by the acquisition of activating acetylation marks, resulting in an overall negative impact on gene expression. Since SENP7-mediated heterochromatin stabilization has been fundamentally shown for pericentric heterochromatin [20], which is classified as constitutive heterochromatin, we cannot exclude a different SENP7 behavior on facultative heterochromatin, frequently associated with developmental genes. Indeed, developmental genes usually exist in a poised state, with reduced transcription, although ready for immediate activation. Most of them are defined as bivalents, since they simultaneously contain both activating (H3K4me3) and repressing (H3K27me3) marks in their promoters. Thus, it is tempting to place SENP7 in this scenario, labelling chromatin positions for full opening when required. Notably, ischemic conditions, in which we have previously shown that SENP7 is downregulated [14], lead to reduced histone H3 acetylation, which results in chromatin condensation [39]. Despite the phenotypic rescue shown by the catalytic domain, we cannot exclude the possibility that N-terminal SENP7 is continuously facilitating chromatin association and that stable and constitutive expression of the catalytic domain from a strong promoter overcomes the need for chromatin association in the case of developmental genes. Robust

expression of the reintroduced catalytic domain might also explain why, in the stable cell line, histone H3 acetylation reaches values higher than those of parental cells.

Thus, we have uncovered a dual function for SENP7 in HAP1 cells. We propose that regarding a significant set of developmental genes, SENP7 is required for chromatin opening, a function mainly relying on its isopeptidase activity. By contrast, for chrX genes, and probably for additional genes in other chromosomes, despite the modest upregulation observed in KO cells, SENP7 displays a different relation with chromatin, involving this protease in maintaining a moderate repressive state. This aspect absolutely requires its N-terminal region and is then more related to the previous association of SENP7 with pericentric heterochromatin stabilization [20], which may require the participation of additional chromatin actors, such as the histone variant mH2A. Notably, in the case of chrX, this feature can be exploited for the study of its biology or for therapeutic intervention against diseases linked to chrX condensation.

MATERIALS AND METHODS

Plasmid constructs

The construct for stable integration of the catalytic domain was based on plasmid pAM_1C (Active Motif, Waterloo, Belgium). A DNA fragment coding for amino acids 732–1050 of SENP7 was amplified by PCR and cloned into the *Hin*dIII site of pAM_1C, upstream of the AM tag. A fragment coding for the classical NLS of SV40 virus large T-antigen, corresponding to the amino acid sequence PKKKRKV, was placed at the N-terminus by standard PCR techniques. Construct for misexpression of full-length SENP7 in P19 cells and in embryos has already been described and was based on plasmid pAdRSV-Sp, with a Flag tag at the N-terminus [14]. Constructions for the misexpression of the catalytic domain and an N-terminal fragment of SENP7 were also based on plasmid pAdRSV-Sp, both containing a Flag tag at the N-terminus. The fragment for the catalytic domain was the same as described above, including NLS but lacking the AM tag, while that for the N-terminal fragment included amino acids 1 to 308. Cloning was accomplished by using standard PCR techniques and appropriate enzyme restriction sites. To induce neurogenesis in P19 cells, previously described expression constructs for Neurod2 and its partner E12 were used as explained in [26]. The Neurog2 expression construct used in embryos has also been described [40]. The pEGFP-N1 plasmid (BD Biosciences Clontech, San Jose, CA, USA) was included in all electroporation experiments as a GFP reporter vector.

Cell culture, transfection, and stable cell line

HAP1 parental cells, together with KO1 (HZGHC006875c010) and KO2 (HZGHC006874c003) mutant cells, were obtained from Horizon Discovery (Cambridge, UK), and cultured in Iscove Modified Dulbecco's medium (IMDM) from Gibco (Thermo Fisher Scientific, Waltham, MA, USA), supplemented with 10% fetal bovine serum (FBS) (Sigma-Aldrich, St. Louis, MO, USA). P19 cells were purchased from ATCC (LGC Standards, Barcelona, Spain) and were cultured in α-modified Minimum Essential Medium (α-MEM) (HyClone, Logan, UT, USA) supplemented with 7.5% calf serum (HyClone) and 2.5% FBS (Sigma-Aldrich).

All media were also supplemented with 10 ml/l of an antibiotic solution with Penicillin (100 U/ml) and Streptomycin (10 mg/ml) (Sigma-Aldrich). Transfection of HAP1 and P19 cells was achieved by using the X-tremeGENE 9 (Sigma-Aldrich) and Lipofectamine 2000 (Invitrogen, Life Technologies, Paisley, UK) reagents following the manufacturer's instructions. For stable integration of the pAM_C1-based construct in KO1 cells, 24 h after transfection, the medium was supplemented with 3 μg/ml of puromycin to allow for the appearance of isolated colonies (10–14 days) after death of non-resistant cells.

Western blot

For Western blots, cells were lysed in 50 mM Tris-HCl pH 7.5, 150 mM NaCl, 1% Triton X-100, supplemented with the EDTA-containing complete protease inhibitor cocktail (Sigma-Aldrich). Protein quantification was determined with the Bio-Rad protein assay, based on the Bradford dye-binding method (Bio-Rad, Hercules, CA, USA). After protein separation in SDS-containing polyacrylamide gels, they were transferred to PVDF membranes (GE Healthcare, Buckinghamshire, UK) for antibody incubation. To reveal hybridization, membranes were assayed with the chemiluminescence ECL system (Bio-Rad) and analyzed in a ChemiDoc XRS apparatus (Bio-Rad). The AbFlex AM-Tag antibody (rAb) (#91111, 1:1000, Active Motif) and anti-mouse HRP-conjugated secondary antibodies (1:10000, Sigma-Aldrich) were used.

Embryo electroporation, P19 cells immunofluorescence, imaging and neurogenesis quantification

Electroporation of the embryonic neural tube was carried out as previously described [40]. Briefly, fertilized eggs were incubated at 37°C to the HH13 stage (48–52 h). Plasmids of interest were injected into the neural tube at 1 μg/μl in 10 mM Tris (pH 8.0), together with the reporter GFP plasmid at 0.3 μg/μl. Embryos were electroporated at the thoracic spinal cord level. Electroporation was applied from an ECM 830 Electro Square Porator (BTX, Harvard Apparatus, Holliston, MA, USA) with 6 pulses of 25 V and 50 milliseconds at a frequency of 1 Hz. After electroporation, eggs were incubated again to HH22 (about 36 additional h). Embryos were then harvested in phosphate-buffered saline (PBS), fixed in 4% paraformaldehyde (PFA) in PBS for 3 h, and dehydrated in a methanol series. For immunofluorescence, embryos were rehydrated and embedded in 4% agarose. Fifty μm-thick vibratome sections were prepared and blocked in PBS supplemented with 0.25% Triton X-100 and 5% donkey serum. Primary antibodies were incubated overnight at 4°C in the same solution. Secondary antibodies were incubated at room temperature for 2 hours. Sections were mounted with Vectashield (Vector Laboratories, Inc., Newark, CA, USA). Cell immunofluorescence was conducted in a similar way, seeding cells directly on coverslips and using Triton X-100 at 0.1%. Antibodies: neuron specific marker ßIII-tubulin (rabbit, 1:500, #ab18207, Abcam, Cambridge, UK), AM-Tag (mouse, 1:500, #91111, Active Motif), donkey anti-mouse and anti-rabbit IgG Cy3-conjugated (1:800, #715-165-150 and #711-165-152, Jackson Immunoresearch, Suffolk, UK). Cell nuclei were revealed by DAPI (1:10000, #D9542, Sigma-Aldrich) staining. Cells and embryo images were acquired on Leica Microsystems GmbH (Wetzlar, Germany) epifluorescence DM6000 and confocal TCS SP5II microscopes (Leica Microsystems, Wetzlar, Germany), respectively, and processed with Leica LAS AF and Adobe Photoshop software. Neurogenesis in P19 cells was induced by

transient transfection of Neurod2 and E12 expression vectors, according to [26], and quantified as the % of cells expressing ßIII-tubulin in relation to the total number of cells in a field, as revealed by DAPI. Neurogenesis in the neural tube was induced by Neurog2 forced expression, and quantified as the % of GFP-positive cells located in the ML, as revealed by expression of ßIII-tubulin.

RNA extraction, retrotranscription, genomic DNA extraction, and qPCR

For total RNA extraction from HAP1 cells, to be used in qPCR experiments, we used the NZY Total RNA isolation kit (NZYTech, Lisbon, Portugal). Retrotranscription was achieved with the High-Capacity cDNA Reverse Transcription Kit (Applied Biosystems, Carlsbad, CA, USA). qPCR experiments from total RNA were set up with the Power SYBR Green (Applied Biosystems) in a ViiA7 Real-Time PCR System (Applied Biosystems). The *RPLP0* gene was used as a housekeeping reference to analyze the relative expression of other genes. Normalization was performed as described in [41]. For genomic DNA extraction, 10^6 cells were lysed in 500 µl of 50 mM Tris-HCl pH 7.5, 100 mM NaCl, 0.5% SDS, 5 mM EDTA, supplemented with 100 µg/ml of Proteinase K, overnight at 37 ºC. After isopropanol-mediated precipitation, the pellet was resuspended in 100 µl of 10 mM Tris-HCl pH 8.0, and heated at 95 ºC for 5 min to achieve Proteinase K inactivation. qPCR experiments were performed with 3 µl of this preparation. qPCR data were mean values obtained from three independent experiments plated in triplicate. The primers used are described in the Supplementary Table S1.

RNA-Seq

Total RNA was extracted with the RNeasy kit (QIAGEN, Austin, TX, USA) and processed in CABIMER Genomics facility. Duplicate samples were prepared for each condition. To remove genomic DNA traces, an on-column DNase digestion was performed using the RNase-Free DNase Set (QIAGEN). Total RNA quality was assessed using an Agilent 2100 Bioanalyzer. Strand-specific RNA-seq libraries were prepared from 150 ng of total RNA using the Illumina Stranded Total RNA Prep with Ribo-Zero Plus kit (Illumina, Inc., San Diego, CA, USA) according to the manufacturer's instructions. Libraries were sequenced on an Illumina NovaSeq 6000 platform using 2 × 75 bp paired-end reads, generating approximately 90 million reads per sample.Reads were aligned to the human reference genome (GRCh38/hg38) using the align function from Rsubread v2.20.0 [42]. Gene-level counts were obtained using featureCounts with the hg38 NCBI RefSeq annotation. Lowly expressed genes were filtered using edgeR v4.4.1 [43], retaining genes with CPM > 0.5 in at least two samples. Sample clustering was assessed by multidimensional scaling (MDS) using the plotMDS function from limma based on log-transformed CPM values [44]. Differential gene expression analysis was performed using DESeq2 [45]. PCA was performed using the plotMDS function implemented in the limma-voom package (v3.34.9), based on gene expression values normalized as CPM. Genes that were upregulated or downregulated with a p-value < 0.05 and $|\log2(FC)| > 0.5$ were selected for subsequent analysis. For sashimi plot visualization, RNA-seq reads were independently aligned to the human reference genome (GRCh38/hg38) using STAR [46]. BAM files were indexed using SAMtools [47] and coverage tracks were generated with deepTools using RPKM normalization [48]. Biological replicates from the same condition were merged and Sashimi plots were

generated in IGV [49]. Heatmaps were generated in R using the heatmap.2 function from the gplots package. Gene expression values were represented as z-scores. RNA-seq data have been deposited at the Gene Expression Omnibus (GEO) repository with accession number GSE336434.

DNA compaction analysis, high-content fluorescence microscopy and image analysis

Confocal images were collected in a Leica TCS SP5II confocal laser scanning microscope (Leica Microsystems) equipped with an oil immersion Plan-Apochromat 100x/1.44 NA objective lens (pixel size in XY set to 50 nm, Z-step = 290 nm). Confocal image stacks were preprocessed using a macro made in Fiji/ImageJ 1.54p (National Institutes of Health, Bethesda, MD, USA) and RStudio 2025.09.0 + 387. The high-content fluorescence microscopy images were initially analyzed by Harmony software and Excel, and initial results were analyzed by RStudio. The raw multichannel TIFF files with DAPI, and fluorescence signals were imported and split into individual channels for further processing. A nuclear segmentation channel was generated by duplicating the DAPI signal and Gaussian smoothing ($\sigma = 2$ pixels) to remove high-frequency noise while retaining overall nuclear morphology. The smoothed DAPI images were later segmented using the Otsu automatic thresholding algorithm applied to the whole image stack using a common stack histogram. Then, a hole-filling operation was applied to correct for internal discontinuities within the segmented nuclei, allowing the generation of continuous nuclear objects for downstream image analysis. The processed DAPI-derived segmentation channel was then merged with the original fluorescence channels. Final image stacks were saved as 8-bit greyscale TIFF files and exported for subsequent quantitative analysis. For the 3D analysis of chromatin compaction, nuclei were classified using the 'nucim' image analysis framework as performed in [50, 51], a tool freely available in open-source R packages based on 'bioimagetools'. The processed DAPI-derived mask was utilized for nuclear segmentation and classification based on spatial distribution and intensity characteristics of DAPI signal. The total DNA fraction of individual nuclei was classified into one of seven classes of chromatin compaction ranging from Class 1 (interchromatin active compartments) to Class 7 (compacted core of chromatin clusters, inactive compartments). Subsequently, fluorescence intensity measurements were obtained from the original, unaltered image channels, thereby avoiding biases introduced by segmentation. Quantitative analyses and statistical comparisons were performed per class. In addition to chromatin classification, DAPI-derived measurements were used as surrogate markers of DNA compaction and combined with immunofluorescence staining, performed as described for P19 cells, for the following antibodies: H3K9me3 (mouse, 1:100, #39285, Active Motif), H3K27me3 (rabbit, 1:100, #39155, Active Motif), H3K9ac (mouse, 1:250, #61251 and #61253, Active Motif), H3K27ac (rabbit, 1:200, #8173, Cell Signaling Technology, Leiden, The Netherlands), mH2A1 (rabbit, 1:250, #39593, Active Motif), goat anti-mouse IgG Alexa Fluor 594 (1:800, #A-11005, Thermo Fisher Scientific) and donkey anti-rabbit IgG cy5-conjugated (1:800, #711-175-52, Jackson Immunoresearch). Histone modifications and mH2A1 levels were measured with the Operetta high-content screening system (Perkin Elmer, UK) in wide-field mode, equipped with a Xenon fiber optic light source and a 20x/0.45 NA long working distance or a 40x/0.95 NA objective. For excitation and emission, the following filter combinations were used: 360–400 nm and 410–480 nm for DAPI or AMCA, 460–490 nm and 500–550 nm for GFP or Alexa-488

as well as 560–580 nm and 590–640 nm for TexasRed or Alexa-594. Fluorescence intensity levels were quantified with the Harmony software (Version 3.5.1, PerkinElmer, UK).

Statistical analysis and other tools

Statistical analysis of the results was accomplished with the Prism 11.0.2 (GraphPad) software. Bar charts show mean values ± s.d. from 3 independent determinations. One-way ANOVA ($p < 0.05$) implemented with the Tukey post-test for multiple comparisons was used for statistical analysis of different groups (*$p < 0.05$, **$p < 0.01$, ***$p < 0.001$). Paired and unpaired Student's *t*-test were applied for the analysis of scatter plots and embryo immunofluorescence quantifications, respectively, as indicated. For all data, we assumed a normal distribution and similar variances. The Venny tool 2.1 at https://bioinfogp.cnb.csic.es/tools/venny was used to analyze overlaps between different data sets. The significance of the overlaps observed in Venn diagrams was analyzed by applying the hypergeometric test at https://systems.crump.ucla.edu/hypergeometric/. Venn diagrams were drawn to scale at https://www.meta-chart.com/venn#/display. GO functional categories were established through the DAVID tool [52] at https://davidbioinformatics.nih.gov/.

DATA AVAILABILITY

Transcriptomic data comparisons are provided in Supplementary Dataset S1. Data have been deposited at GEO (https://www.ncbi.nlm.nih.gov/geo/), under accession number GSE336434. Uncropped images of western blots are provided in the Supplementary File Uncropped WB.

Declarations

COMPETING INTEREST

The authors declare no competing interests.

ETHICS APPROVAL AND CONSENT TO PARTICIPATE

All methods used were carried out in accordance with relevant guidelines and regulations. This study involves the use of cell lines and 3.5-day chick embryos, which do not require ethical approval. No other samples, material, or data from human or animal origin sensitive to ethical considerations have been used.

AUTHOR CONTRIBUTIONS

VJ conducted most experiments. BT-A and NL-U conducted some experiments. LG-B performed transcriptomic data analysis, supervised by JCR supervised, who also edited the manuscript. MA supervised confocal and high-content microscopy analyses and edited the manuscript. MCC participated in experimental design, data analysis, funding acquisition, and manuscript editing. MG-D

performed conceptualization, supervision, data analysis, funding acquisition, visualization, graphics and figures preparation, and manuscript writing. All authors read and approved the final manuscript.

ACKNOWLEDGMENTS

This work was supported by MICIN/AEI/10.13039/ 501100011033, Spain/ERDF “A way to make Europe”, European Union, Grant no. PID2024-159091NB-I00 to MGD, and by the Deutsche Forschungsgemeinschaft (DFG, German Research Foundation) – Project-ID 393547839 – SFB 1361 to M.C.C.

References

1. Vertegaal ACO. Signalling mechanisms and cellular functions of SUMO. Nat Rev Mol Cell Biol. 2022;23:715–31.
2. Martin-Rufo R, Gomez-Moya A, Lecona E. The SUMO Pathway. Methods Mol Biol. 2025;2957:1–15.
3. Kunz K, Piller T, Muller S. SUMO-specific proteases and isopeptidases of the SENP family at a glance. J Cell Sci. 2018;131.
4. Li Y, De Bolos A, Amador V, Reverter D. Structural Basis for the SUMO2 Isoform Specificity of SENP7. J Mol Biol. 2022;434:167875.
5. Lima CD, Reverter D. Structure of the human SENP7 catalytic domain and poly-SUMO deconjugation activities for SENP6 and SENP7. J Biol Chem. 2008;283:32045–55.
6. Claessens LA, Verlaan-de Vries M, de Graaf IJ, Vertegaal ACO. SENP6 regulates localization and nuclear condensation of DNA damage response proteins by group deSUMOylation. Nat Commun. 2023;14:5893.
7. Fu H, Liu N, Dong Q, Ma C, Yang J, Xiong J, et al. SENP6-mediated M18BP1 deSUMOylation regulates CENP-A centromeric localization. Cell Res. 2019;29:254–7.
8. Liebelt F, Jansen NS, Kumar S, Gracheva E, Claessens LA, Verlaan-de Vries M, et al. The poly-SUMO2/3 protease SENP6 enables assembly of the constitutive centromere-associated network by group deSUMOylation. Nat Commun. 2019;10:3987.
9. Mukhopadhyay D, Arnaoutov A, Dasso M. The SUMO protease SENP6 is essential for inner kinetochore assembly. J Cell Biol. 2010;188:681–92.
10. Wagner K, Kunz K, Piller T, Tascher G, Holper S, Stehmeier P, et al. The SUMO Isopeptidase SENP6 Functions as a Rheostat of Chromatin Residency in Genome Maintenance and Chromosome Dynamics. Cell Rep. 2019;29:480 – 94 e5.
11. Amrute-Nayak M, Gand LV, Khan B, Holler T, Kefalakes E, Kosanke M, et al. SENP7 deSUMOylase-governed transcriptional program coordinates sarcomere assembly and is targeted in muscle atrophy. Cell Rep. 2022;41:111702.

12. Cui Y, Yu H, Zheng X, Peng R, Wang Q, Zhou Y, et al. SENP7 Potentiates cGAS Activation by Relieving SUMO-Mediated Inhibition of Cytosolic DNA Sensing. PLoS Pathog. 2017;13:e1006156.
13. Gallardo-Chamizo F, Gonzalez-Prieto R, Jafari V, Luna-Pelaez N, Vertegaal ACO, Garcia-Dominguez M. SUMO2/3 modification of transcription-associated proteins controls cell viability in response to oxygen and glucose deprivation-mediated stress. Cell Death Discov. 2025;11:230.
14. Gallardo-Chamizo F, Lara-Urena N, Correa-Vazquez JF, Reyes JC, Gauthier BR, Garcia-Dominguez M. SENP7 overexpression protects cancer cells from oxygen and glucose deprivation and associates with poor prognosis in colon cancer. Genes Dis. 2022;9:1419–22.
15. Garvin AJ, Densham RM, Blair-Reid SA, Pratt KM, Stone HR, Weekes D, et al. The deSUMOylase SENP7 promotes chromatin relaxation for homologous recombination DNA repair. EMBO Rep. 2013;14:975–83.
16. Huang CJ, Wu D, Jiao XF, Khan FA, Xiong CL, Liu XM, et al. Maternal SENP7 programs meiosis architecture and embryo survival in mouse. Biochim Biophys Acta Mol Cell Res. 2017;1864:1195–206.
17. Juarez-Vicente F, Luna-Pelaez N, Garcia-Dominguez M. The Sumo protease Senp7 is required for proper neuronal differentiation. Biochim Biophys Acta. 2016;1863:1490–8.
18. Li X, Jiao F, Hong J, Yang F, Wang L, Gong Z. SENP7 knockdown inhibited pyroptosis and NF-kappaB/NLRP3 inflammasome pathway activation in Raw 264.7 cells. Sci Rep. 2020;10:16265.
19. Maison C, Romeo K, Bailly D, Dubarry M, Quivy JP, Almouzni G. The SUMO protease SENP7 is a critical component to ensure HP1 enrichment at pericentric heterochromatin. Nat Struct Mol Biol. 2012;19:458–60.
20. Romeo K, Louault Y, Cantaloube S, Loiodice I, Almouzni G, Quivy JP. The SENP7 SUMO-Protease Presents a Module of Two HP1 Interaction Motifs that Locks HP1 Protein at Pericentric Heterochromatin. Cell Rep. 2015;10:771–82.
21. Samra N, Jansen NS, Morani I, Kakun RR, Zaid R, Paperna T, et al. Exome sequencing links the SUMO protease SENP7 with fatal arthrogryposis multiplex congenita, early respiratory failure and neutropenia. J Med Genet. 2023;60:1133–41.
22. Suhail A, Rizvi ZA, Mujagond P, Ali SA, Gaur P, Singh M, et al. DeSUMOylase SENP7-Mediated Epithelial Signaling Triggers Intestinal Inflammation via Expansion of Gamma-Delta T Cells. Cell Rep. 2019;29:3522–38 e7.
23. Wu Z, Huang H, Han Q, Hu Z, Teng XL, Ding R, et al. SENP7 senses oxidative stress to sustain metabolic fitness and antitumor functions of CD8 + T cells. J Clin Invest. 2022;132.
24. Zhu H, Ren S, Bitler BG, Aird KM, Tu Z, Skordalakes E, et al. SPOP E3 Ubiquitin Ligase Adaptor Promotes Cellular Senescence by Degrading the SENP7 deSUMOylase. Cell Rep. 2015;13:1183–93.
25. Banerjee R, Sotero-Caio CG, Fu B, Yang F. Chromosomal instability (CIN) in HAP1 cell lines revealed by multiplex fluorescence in situ hybridisation (M-FISH). Mol Cytogenet. 2022;15:46.
26. Farah MH, Olson JM, Sucic HB, Hume RI, Tapscott SJ, Turner DL. Generation of neurons by transient expression of neural bHLH proteins in mammalian cells. Development. 2000;127:693–702.

27. Smeets D, Markaki Y, Schmid VJ, Kraus F, Tattermusch A, Cerase A, et al. Three-dimensional super-resolution microscopy of the inactive X chromosome territory reveals a collapse of its active nuclear compartment harboring distinct Xist RNA foci. Epigenetics Chromatin. 2014;7:8.
28. Chadwick BP, Willard HF. Histone H2A variants and the inactive X chromosome: identification of a second macroH2A variant. Hum Mol Genet. 2001;10:1101–13.
29. Li J, Ming Z, Yang L, Wang T, Liu G, Ma Q. Long noncoding RNA XIST: Mechanisms for X chromosome inactivation, roles in sex-biased diseases, and therapeutic opportunities. Genes Dis. 2022;9:1478–92.
30. Rytinki MM, Kaikkonen S, Pehkonen P, Jaaskelainen T, Palvimo JJ. PIAS proteins: pleiotropic interactors associated with SUMO. Cell Mol Life Sci. 2009;66:3029–41.
31. Claessens LA, Vertegaal ACO. SUMO proteases: from cellular functions to disease. Trends Cell Biol. 2024.
32. Kobayashi ES, Lotan NS, Schejter YD, Makowski C, Kraus V, Ramchandar N, et al. Biallelic Loss of Function Variants in SENP7 Cause Immunodeficiency with Neurologic and Muscular Phenotypes. J Pediatr. 2024;274:114180.
33. Kotecha U, Kim ES, Shah PS, Shah N, Gupta VA. A Splice Site Variant in SENP7 Results in a Severe Form of Arthrogryposis. Clin Genet. 2025;107:688–93.
34. Pal P, Nerakh G, Bhat S, Siby E, Undamatla V, Vavilala S, et al. SENP7-Related Fatal Arthrogryposis Multiplex Congenita and Immunodeficiency: A Novel Missense Variation and Syndromic Delineation. Clin Genet. 2025;108:752–4.
35. Saad AK, Hassan NH, Soliman HN, Zaki MS, Senousy SM, El-Dessouky SH. Lethal Phenotype and Expansion of the Clinical Spectrum of Biallelic Loss of Function Variant in SENP7 Gene Unveiled by Whole Exome Sequencing. Clin Genet. 2025;107:673–9.
36. Cimarosti H, Ashikaga E, Jaafari N, Dearden L, Rubin P, Wilkinson KA, et al. Enhanced SUMOylation and SENP-1 protein levels following oxygen and glucose deprivation in neurones. J Cereb Blood Flow Metab. 2012;32:17–22.
37. Aizawa E, Kaufmann C, Sting S, Boigner S, Freimann R, Di Minin G, et al. Haploid mouse germ cell precursors from embryonic stem cells reveal Xist activation from a single X chromosome. Stem Cell Reports. 2022;17:43–52.
38. Heard E, Rougeulle C, Arnaud D, Avner P, Allis CD, Spector DL. Methylation of histone H3 at Lys-9 is an early mark on the X chromosome during X inactivation. Cell. 2001;107:727–38.
39. Kirmes I, Szczurek A, Prakash K, Charapitsa I, Heiser C, Musheev M, et al. A transient ischemic environment induces reversible compaction of chromatin. Genome Biol. 2015;16:246.
40. Garcia-Dominguez M, Poquet C, Garel S, Charnay P. Ebf gene function is required for coupling neuronal differentiation and cell cycle exit. Development. 2003;130:6013–25.
41. Pfaffl MW. A new mathematical model for relative quantification in real-time RT-PCR. Nucleic Acids Res. 2001;29:e45.

42. Liao Y, Smyth GK, Shi W. The Subread aligner: fast, accurate and scalable read mapping by seed-and-vote. Nucleic Acids Res. 2013;41:e108.
43. Robinson MD, McCarthy DJ, Smyth GK. edgeR: a Bioconductor package for differential expression analysis of digital gene expression data. Bioinformatics. 2010;26:139–40.
44. Ritchie ME, Phipson B, Wu D, Hu Y, Law CW, Shi W, et al. limma powers differential expression analyses for RNA-sequencing and microarray studies. Nucleic Acids Res. 2015;43:e47.
45. Love MI, Huber W, Anders S. Moderated estimation of fold change and dispersion for RNA-seq data with DESeq2. Genome Biol. 2014;15:550.
46. Dobin A, Davis CA, Schlesinger F, Drenkow J, Zaleski C, Jha S, et al. STAR: ultrafast universal RNA-seq aligner. Bioinformatics. 2013;29:15–21.
47. Morgan M, Pagés H, Obenchain V, Hayden N. Rsamtools: Binary alignment (BAM), FASTA, variant call (BCF), and tabix file import. Bioconductor. 2026.
48. Ramirez F, Ryan DP, Gruning B, Bhardwaj V, Kilpert F, Richter AS, et al. deepTools2: a next generation web server for deep-sequencing data analysis. Nucleic Acids Res. 2016;44:W160-5.
49. Thorvaldsdottir H, Robinson JT, Mesirov JP. Integrative Genomics Viewer (IGV): high-performance genomics data visualization and exploration. Brief Bioinform. 2013;14:178–92.
50. Arroyo M, Casas-Delucchi CS, Pabba MK, Prorok P, Pradhan SK, Rausch C, et al. Histone variant macroH2A1 regulates synchronous firing of replication origins in the inactive X chromosome. Nucleic Acids Res. 2024;52:11659–88.
51. Schmid VJ, Cremer M, Cremer T. Quantitative analyses of the 3D nuclear landscape recorded with super-resolved fluorescence microscopy. Methods. 2017;123:33–46.
52. Huang da W, Sherman BT, Lempicki RA. Systematic and integrative analysis of large gene lists using DAVID bioinformatics resources. Nat Protoc. 2009;4:44–57.

Figures

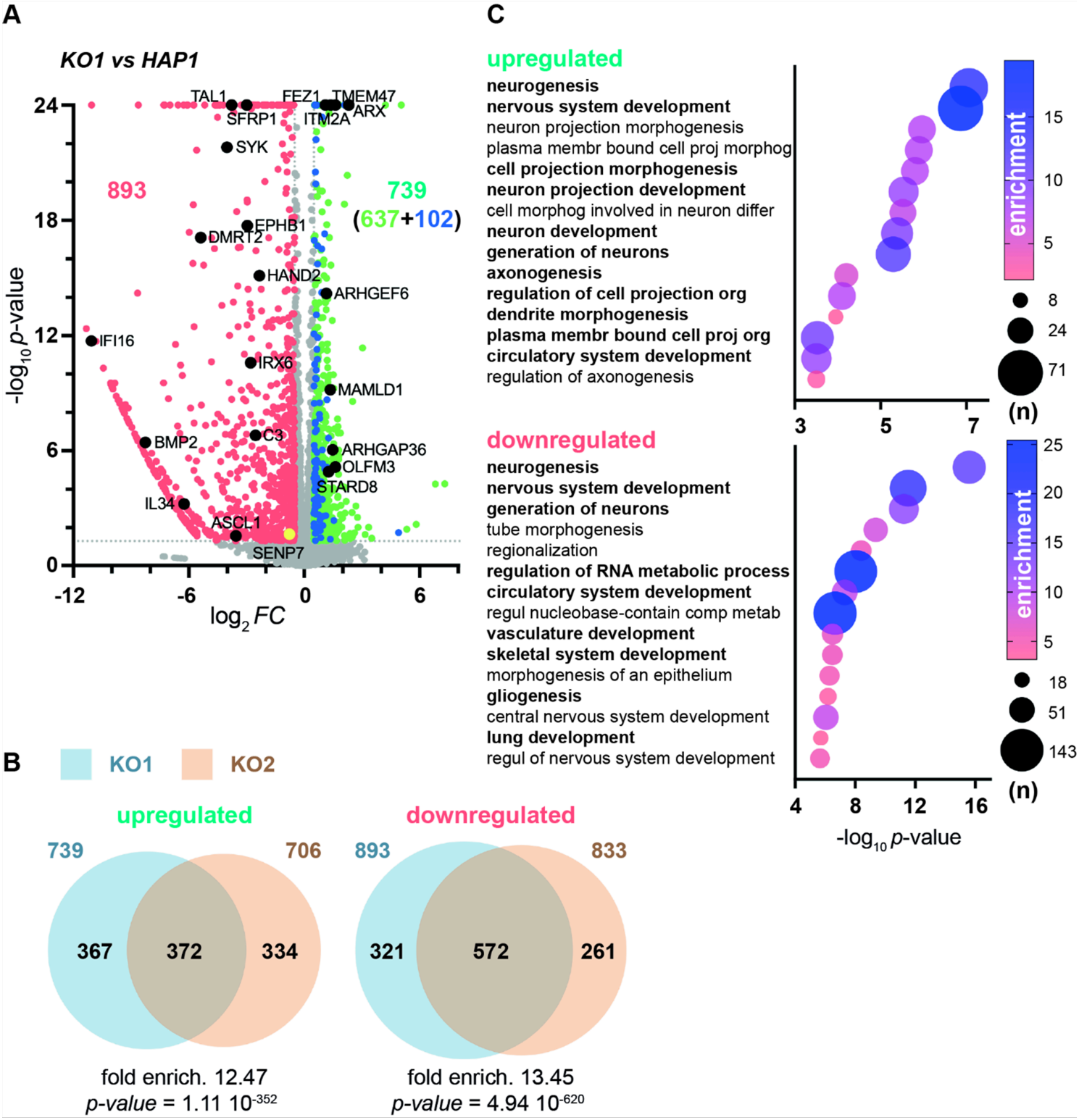


Figure 1

A manifest gene downregulation is observed in *SENP7* KO cells. AVolcano plot of differentially expressed genes (DEGs) in *SENP7* KO cells (KO1) in relation to parental HAP1 cells, generated upon RNA-seq analysis. DEGs out of *p*-value and fold change (FC) cutoffs are in grey. Downregulated genes are represented in red, and upregulated genes in blue (chrX genes) and green (rest of genes). Selected genes are highlighted in black. *SENP7*appears in yellow. The number of misregulated genes in each

category is also indicated. **B** Overlapping of DEGs between KO1 and KO2 cells is represented by a Venn diagram. Numbers on top of the diagram denote the total number of DEGs in each condition. Fold enrichment of the overlapping and the associated *p*-value, as determined by the hypergeometric test, are also indicated below. **C** Gene Ontology (GO) analysis of DEGs in KO1 cells, both upregulated and downregulated, was represented by bubble graphics. Bubble size represents the number of genes in each category as indicated in the legend (n). Color indicates enrichment as indicated in the legend. Top-15 categories according to *p*-values (Benjamini) are shown.

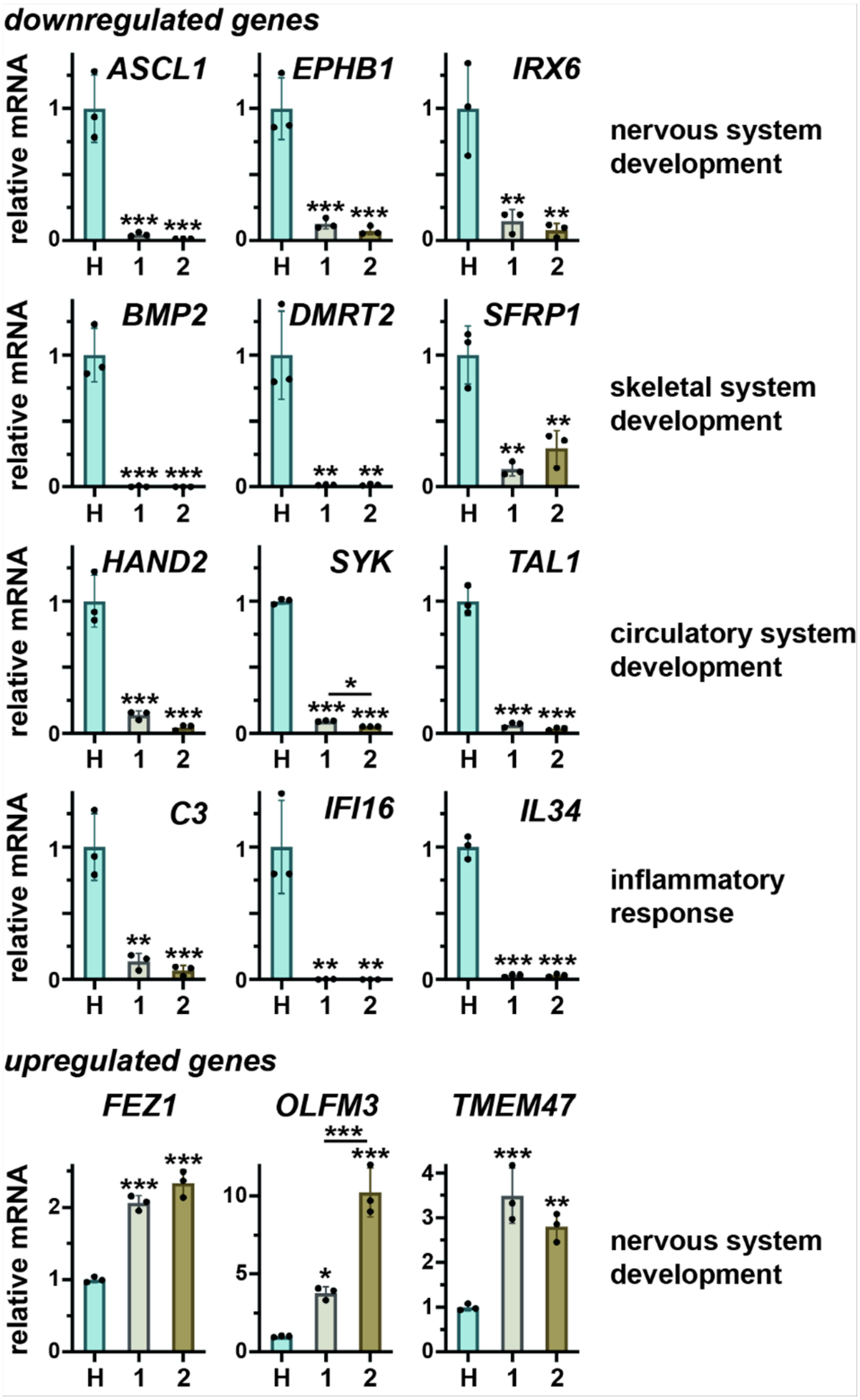


Figure 2

SENP7 is linked to the expression of developmental genes. Results from RNA-seq were validated for a selection of DEGs, both upregulated and downregulated, by quantitative PCR (qPCR). Relative mRNA levels of parental HAP1 (H), KO1(1) and KO2 (2) are represented. Values correspond to mean values ± s.d. from 3 independent experiments analyzed in duplicate. DEGs are grouped in different categories according to their main function, although some of them overlap with several categories (see Supplementary Fig. S2C). Statistical significance of differences was analyzed by one-way ANOVA ($p < 0.05$) followed by Tukey's post-test: * $p < 0.05$, ** $p < 0.01$, *** $p < 0.001$. Differences with parental HAP1 cells are indicated on top of each bar; other differences are indicated with a line.

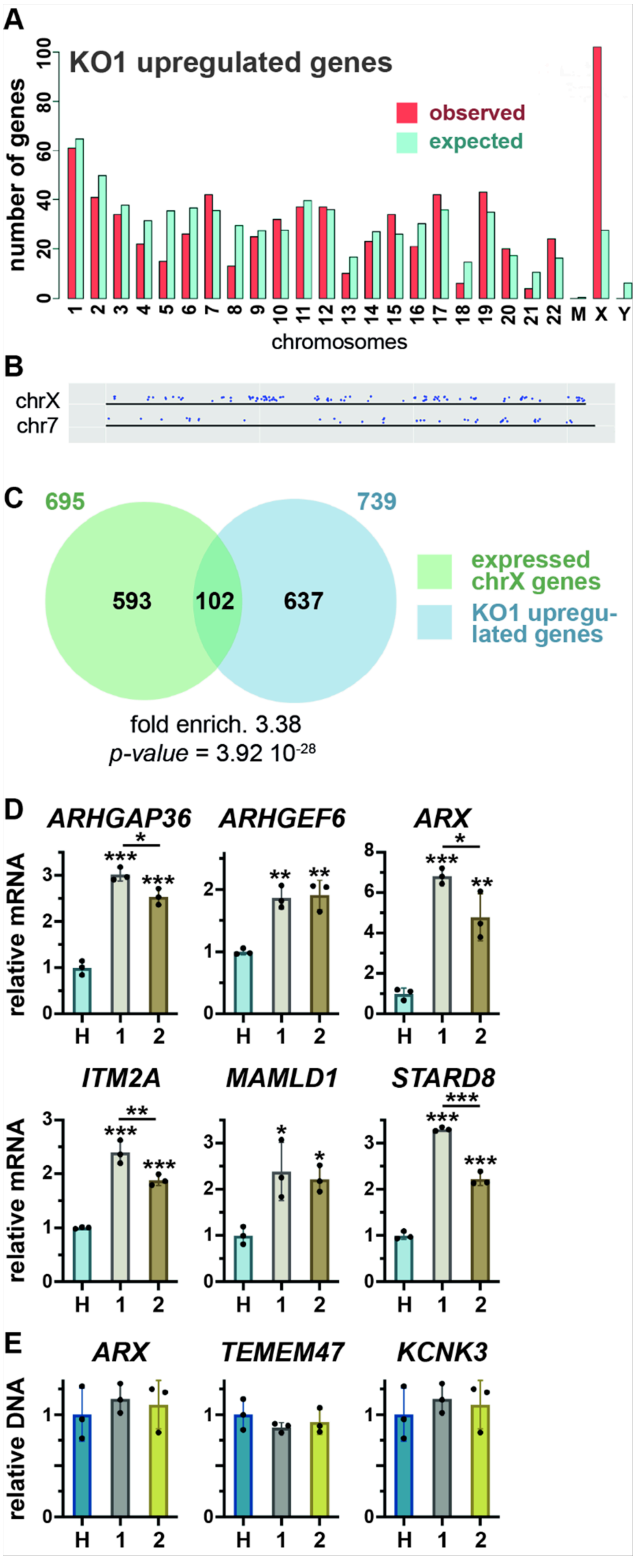


Figure 3

SENP7 loss results in modest upregulation of multiple chromosome X genes. A Bar diagram representing the expected number of upregulated DEGs per chromosome, according to the number of genes on each of them, and the observed value for upregulated DEGs in KO1 cells. **B** Diagram showing the linear distribution of upregulated DEGs along chrX. Upregulated DEGs in chromosome 7 (chr7) are also shown for comparison with a chromosome of similar size. **C** Venn diagram representation of the

overlap between the 695 genes of chrX expressed in HAP1 cells and the 739 genes upregulated in KO1 cells. Fold enrichment and the associated *p*-value of the overlap, determined by the hypergeometric test, are also shown. **D**qPCR validation of results from RNA-seq for a selection of chrX upregulated DEGs. Relative mRNA levels of parental HAP1 (H), KO1(1) and KO2 (2) cells are represented. Values correspond to mean values ± s.d. from 3 independent experiments analyzed in duplicate. Statistical significance of differences was analyzed as in Fig. 2. **E** qPCR assessment of the relative quantity of genomic DNA of parental HAP1 (H), KO1(1) and KO2 (2) cells, analyzed at different loci, 2 located on chrX(*ARX*, *TMEM47*) and 1 located on chr2 (*KCNK3*). Differences, analyzed by one-way ANOVA ($p < 0.05$) and Tukey's post-test, were not significant.

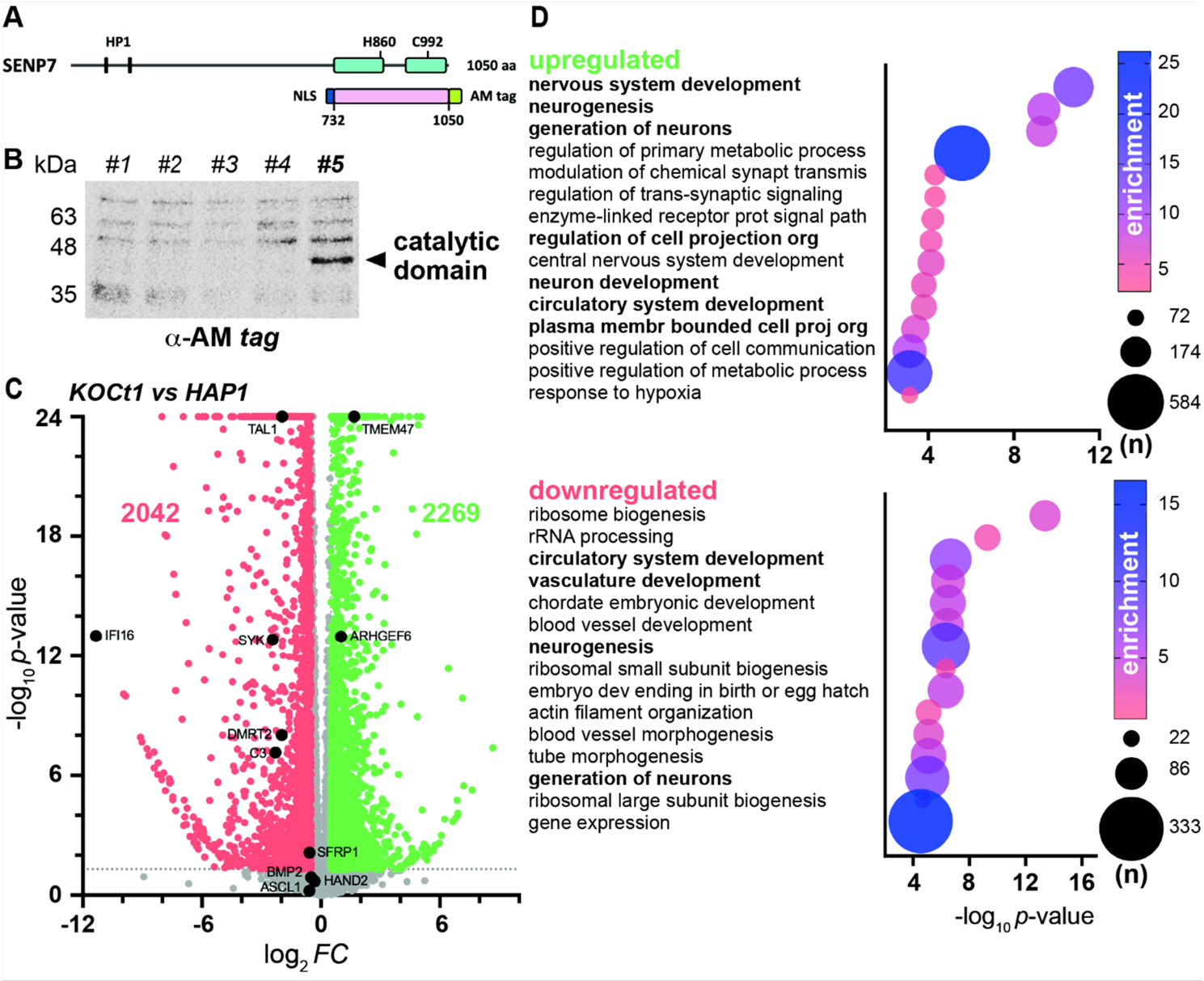


Figure 4

Restoring the catalytic domain of SENP7 in KO cells modifies the expression profile of developmental genes. A Schematic representation of SENP7, showing the split catalytic domain and the construction

used to generate the stable cell line expressing the catalytic domain, labelled with the AM tag, and harboring an N-terminal nuclear localization signal (NLS). Amino acid (aa) positions, key residues of the catalytic domain and the HP1-interacting motifs, are also shown. **B**Western blot analysis of different puromycin-resistant clones obtained after introduction of the catalytic domain construct in KO1 cells, tested with the anti-AM antibody. Only clone #5 expresses the catalytic domain and was designated KOCt1. **C** Volcano plot of DEGs in KOCt1 cells in relation to HAP1 cells, generated after RNA-seq analysis. DEGs out of *p*-value and fold change (FC) cutoffs are in grey. Downregulated genes are represented in red, and upregulated genes in green. Selected genes are highlighted in black. The number of DEGs in each category is also indicated. **D** GO analysis of DEGs in KOCt1 cells, both upregulated and downregulated, represented by bubble graphics. Size of bubbles and color represent the number of genes in each category (n) and enrichment, respectively, as indicated in the legend. Top-15 categories according to *p*-values (Benjamini) are shown.

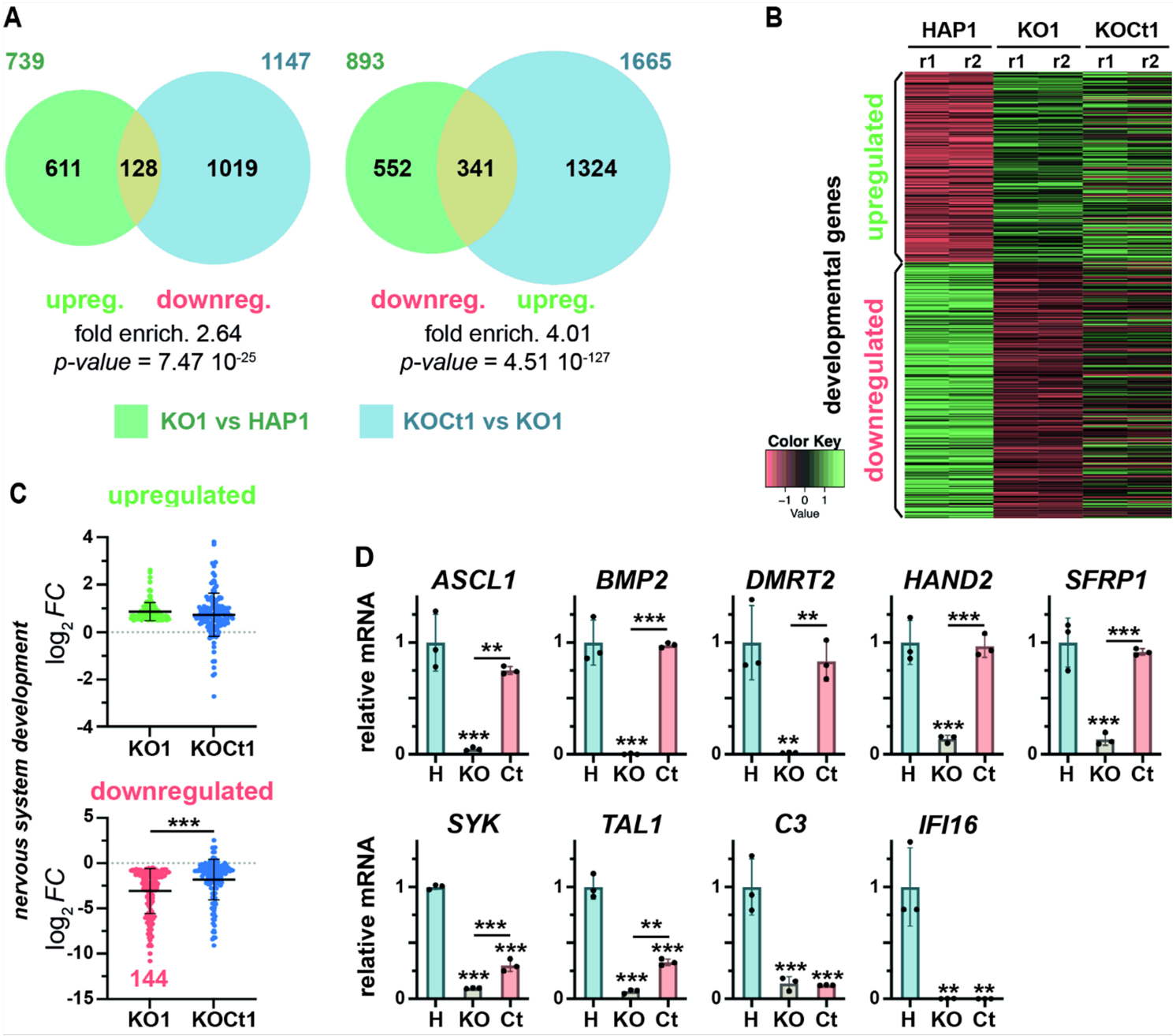


Figure 5

The catalytic domain of SENP7 reverses the downregulation of development-related genes. A Venn diagram of the overlap between DEGs upregulated in KO1 cells compared with HAP1 cells, and DEGs downregulated in KOCt1 cells compared with KO1 cells (left) and the other way around (right). Numbers on top indicate the total number of DEGs in each condition. Fold enrichment of the overlapping and its associated *p*-value, determined by the hypergeometric test, are indicated. **B** Heatmap derived from RNA-seq data, including upregulated and downregulated genes in KO1 cells, compared with their expression in KOCt1 cells. 177 upregulated and 240 downregulated genes from the different developmental GO categories among the top 60 categories (based on Benjamini *p*-value) of genes misregulated in KO1 cells were represented. Genes upregulated and downregulated in KO1 cells are in green and red, respectively. The two experimental RNA-seq replicates (r1, r2) are shown. **C** Scatter plots of the FC of DEGs related to *nervous system development* (*nsd*) in the indicated cells. The FC of upregulated and downregulated *nsd*-related DEGs in KO1 cells was compared with the FC of these genes in KOCt1 cells by paired *t*-test (*** $p < 0.001$; n.s., not significant). **D**Relative mRNA levels of a selection of genes related to *development* and *inflammatory response* were assessed by RT-qPCR in HAP1 (H), KO1(KO) and KOCt1 (Ct) cells. Represented values are mean values ± s.d. from 3 independent experiments analyzed in duplicate. Note that values for HAP1 and KO1 cells are the same as in Fig. 2. Statistical significance of differences was analyzed as in Fig. 2.

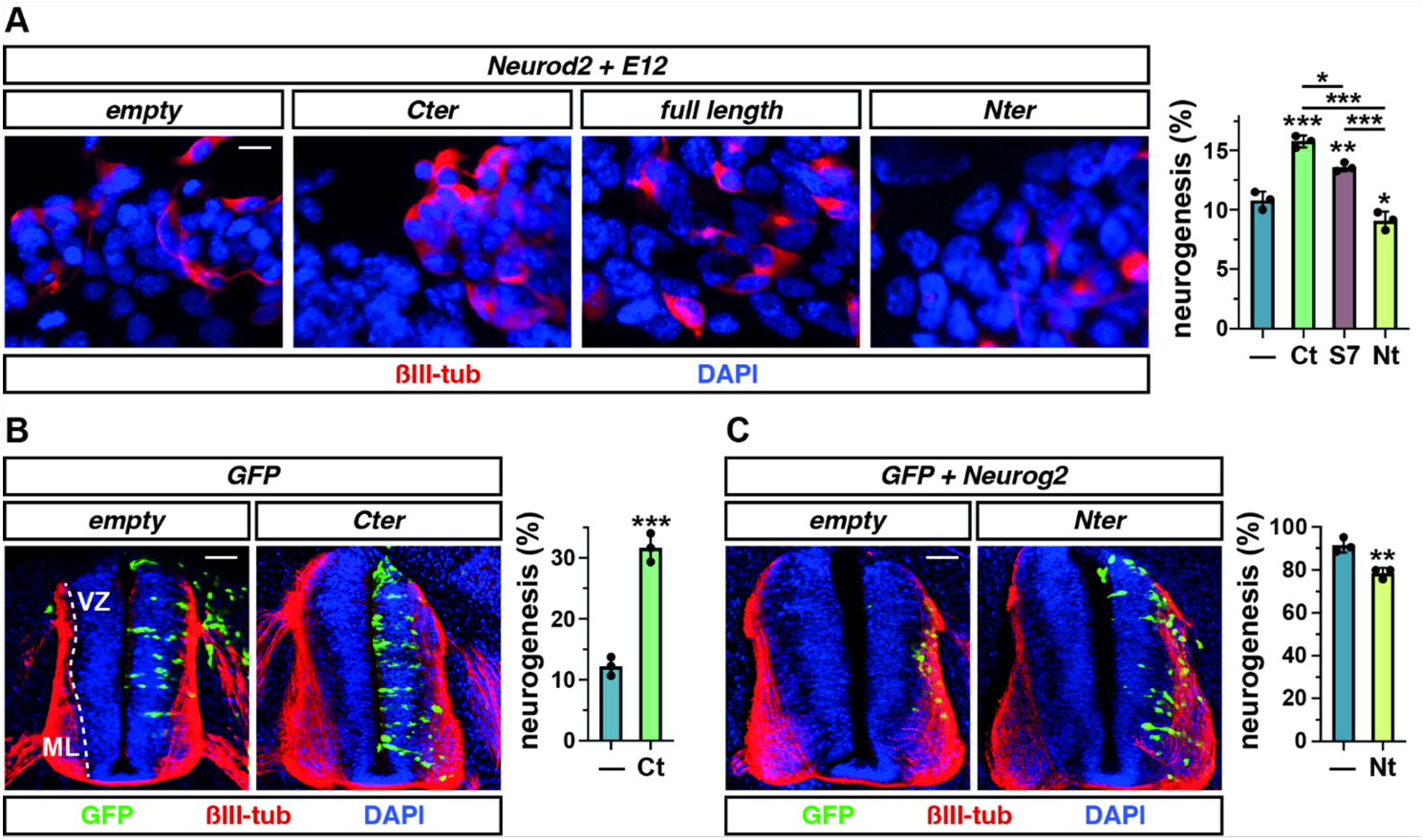


Figure 6

The SENP7 catalytic domain stimulates neurogenesis. A The percentage of neurogenesis driven by the neurogenic factor Neurod2 and its cofactor E12 was evaluated in P19 cells in the presence of different SENP7-derived fragments as indicated: no protein (empty vector, empty, –), catalytic domain (Cter, Ct), full-length SENP7 (full length, S7), and 308 N-terminal amino acids of SENP7 (Nter, Nt). Neurogenesis was calculated as the % of cells expressing the neuronal marker ßIII-tubulin of the total number of cells in the field, as determined by DAPI staining of nuclei. Graph corresponds to the analysis of at least 300 cells per condition from 3 independent experiments performed in duplicate. Scale bar: 10 µm. **B** Naturally occurring neurogenesis was evaluated in the developing chick neural tube by electroporation, in the absence (empty vector, empty, –) or the presence of the SENP7 catalytic domain (Cter, Ct). **C** Electroporation-mediated Neurog2-driven neurogenesis in the neural tube was analyzed in the absence (empty vector, empty, –), or the presence of the SENP7 N-terminal construct (Nter, Nt). **B, C**Neurogenesis was calculated as the % of GFP-positive cells located in the mantle layer (ML), as defined by expression of the neuronal marker ßIII-tubulin, related to the total number of GFP-positive cells in ML and ventricular zone (VZ). Graphs correspond to the analysis of at least 175 cells per condition from several sections of a total of 6 electroporated embryos from 2 independent experiments. A GFP reporter vector was included in all electroporations to monitor the electroporated cells. Scale bars: 30 µm. **A-C** Graphs display mean values ± s.d. Statistical analysis was performed by one-way ANOVA ($p < 0.05$) followed by Tukey's post-test (A) or unpaired *t*-test (B, C): * $p < 0.05$, ** $p < 0.01$, *** $p < 0.001$. Differences with the control condition (empty vector, empty, –) are indicated on top of each bar; other differences are indicated with a line.

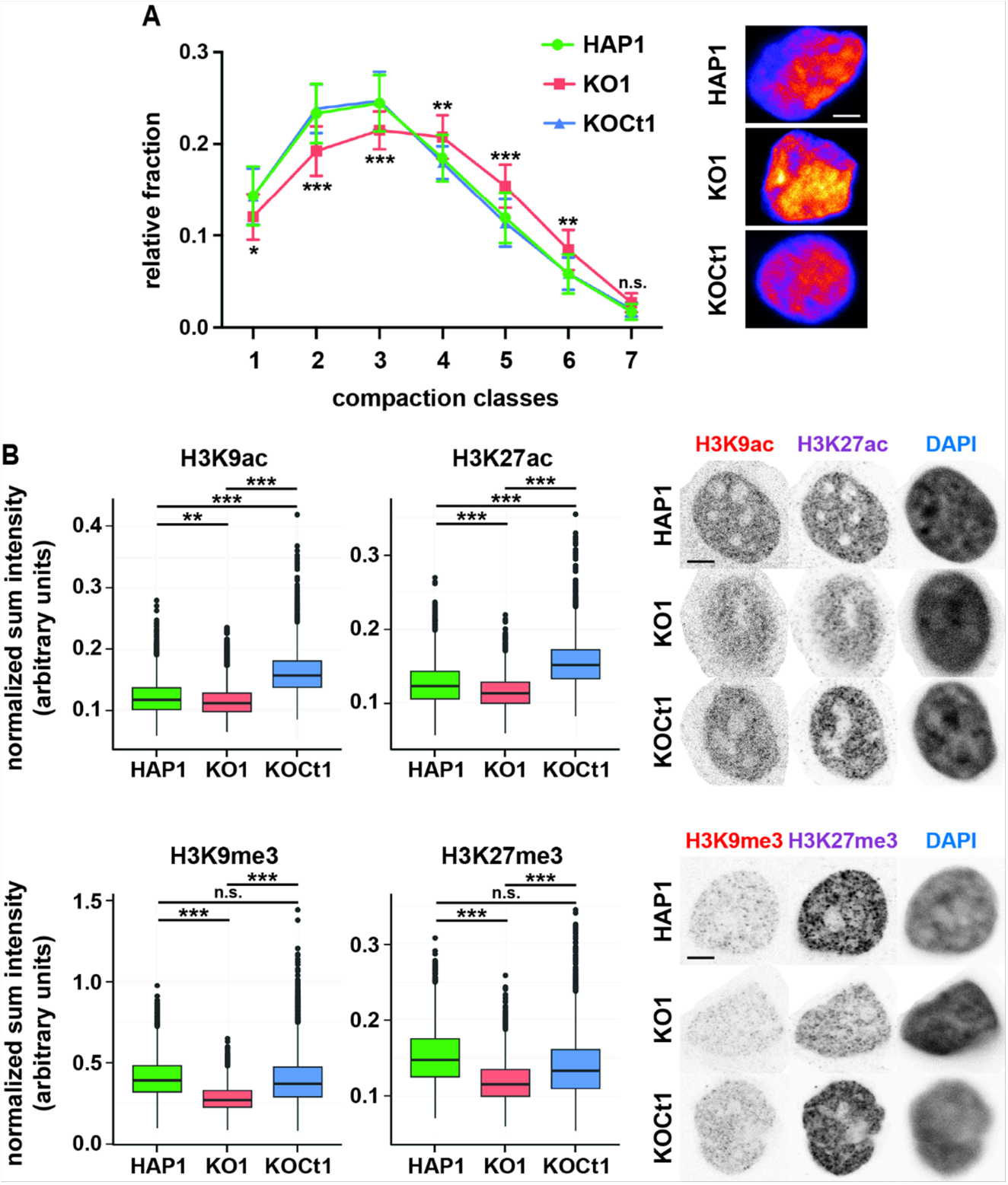


Figure 7

Lack of SENP7 results in altered chromatin structure. A DNA compaction was analyzed in HAP1, KO1, and KOCt1 cells by DAPI staining through distribution of cells in 7 classes according to DAPI staining, corresponding to interchromatin more active compartments (Class 1) to more compacted inactive compartments (Class 7). Data and statistical analysis (ANOVA test, $p < 0.05$) are based on the analysis of 20 randomly selected cells per cell line. Cell lines were compared within each compaction class. No

significant differences were observed between HAP1 and KOCt1 cells. The indicated differences correspond to the comparison of these cell lines with KO1 cells. Representative confocal images for the three cell lines are also shown. Scale bar: 5 μm. Images correspond to grayscale DAPI images converted to Fire in ImageJ. **B** Relative quantity of the indicated histone modifications was analyzed in HAP1, KO1 and KOCt1 cells by high-content fluorescence microscopy. For each nucleus, the total sum intensity of each histone modification was normalized by total DAPI sum intensity. Data are based on the analysis of 5000 cells per cell line. The ANOVA test ($p < 0.05$) was applied for statistical analysis of 300 randomly selected cells. Differences between cells are indicated with a line. **A, B** * $p < 0.05$; ** $p < 0.01$; *** $p < 0.001$; n.s., not significant. A gallery of representative images in grayscale for the different cell lines showing the nuclear distribution and levels of the signal obtained with the indicated antibodies, together with DAPI signal, is also shown. Scale bar: 5 μm.

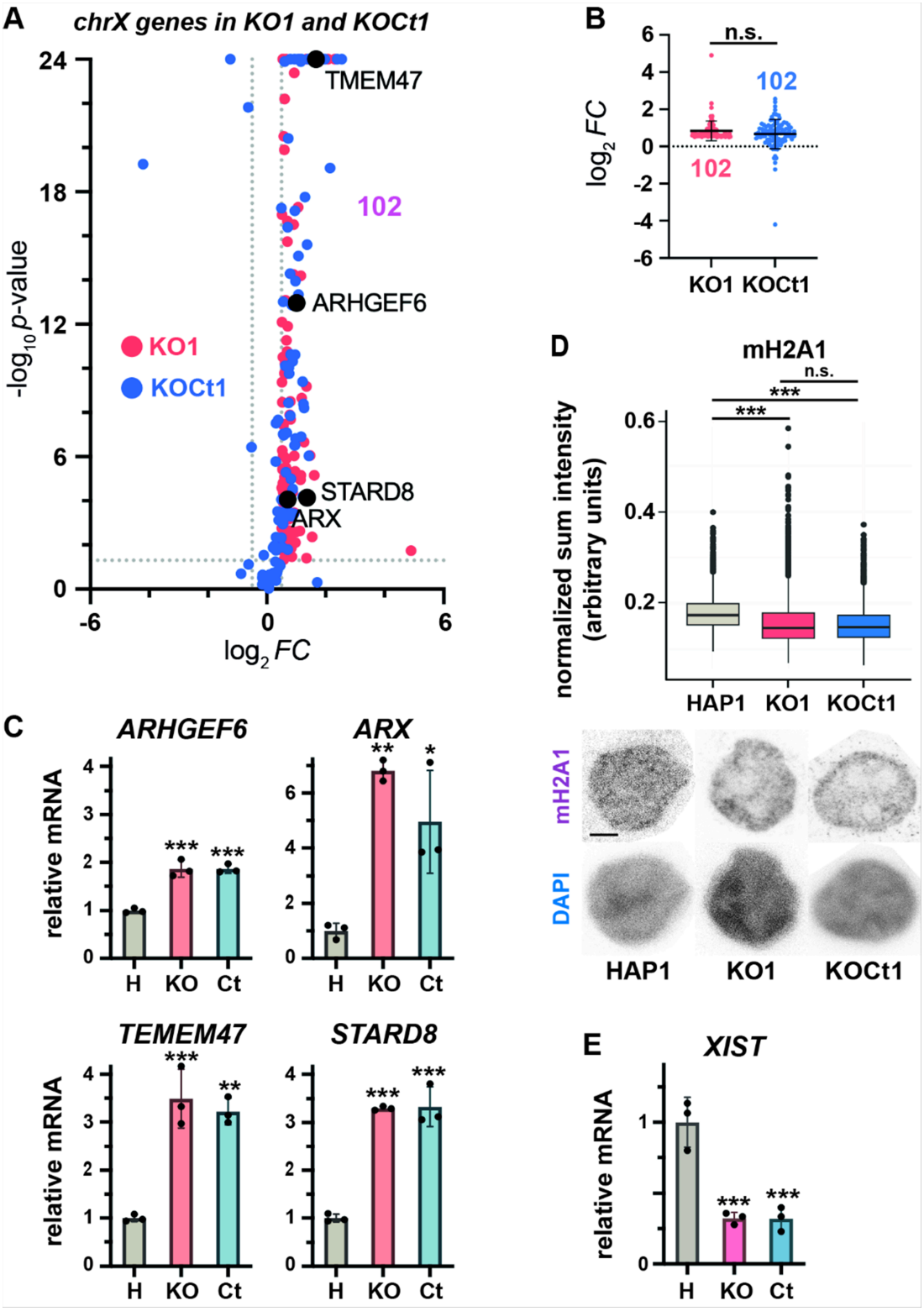


Figure 8

Normal expression of chromosome X genes requires N-terminal SENP7. A Volcano plot showing the distribution of the 102 chrX upregulated DEGs in KO1 cells, and how they distribute in KOCt1 cells, colored in red and blue, respectively. Selected DEGs are highlighted in black. **B** Scatter plot for comparison of the FC of the indicated 102 genes in KO1 and KOCt1 cells. **C** Relative mRNA levels of the indicated genes in HAP1 (H), KO1 (KO), and KOCt1 (Ct) cells, analyzed by qPCR. Note that values for

HAP1 and KO1 cells are the same as in Figs. 2 and 3D for the indicated genes. **D** Relative quantity of the histone variant mH2A1 was analyzed in the indicated cells by high-content fluorescence microscopy as described in Fig. 7B. Representative images for the different cell lines, as indicated in Fig. 7B, are also shown. Scale bar: 5 µm. **E**Relative expression of the lncRNA *XIST* in the indicated cells, analyzed by qPCR. **C, E** Data are mean values ± s.d. from 3 independent experiments analyzed in duplicate. B-E Statistical significance of the differences was established through paired *t*-test (B) or ANOVA ($p < 0.05$) (C-E). Differences are indicated as follows: on top of each bar in relation to HAP1 cells (C, E), with a line between samples (B, D). * $p < 0.05$; ** $p < 0.01$; *** $p < 0.001$; n.s., not significant.

Supplementary Files

This is a list of supplementary files associated with this preprint. Click to download.

- SupplementaryTableS1.docx
- SupplementaryDatasetS1.xlsx
- UncroppedWB.pdf
- SupplementaryFigures.pdf